

1 Introduction

Strain and strain rate imaging are constantly developing techniques in echocardiographic clinical, pre-clinical and basic research. It has been successfully applied in human medicine and more recently in animal experimentation. This technique allows assessment of longitudinal, radial and circumferential component of myocardial function, strain and strain rate, both globally and in individual segments of the myocardium. Additionally, speckle tracking can be used to define rotation of the base and apex and torsion of the left ventricle. STR-derived echocardiography has the potential to quantify left ventricle (LV) systolic and diastolic performance more accurately comparing to conventional 2D echocardiography, as described in number of papers [11, 13, 15].

Nevertheless, despite of substantial research in ultrasound instrumentation and image processing techniques, the utilization of strain analysis is still questionable, due to their limitations. In echocardiography, the strain can be determined by either tissue Doppler techniques or 2D speckle tracking (STR) techniques. This paper is focused on speckle tracking techniques, which have been in center of main interest during the last two decades. The accuracy of these techniques has been widely studied and compared with sonomicrometry and cardiac tagged MRI. The limitations are mainly defined by image quality and temporal resolution [12] and the presence of reverberations. The method therefore suffers from high results variability (consisting of method limitation, inter- and intra-observer variability [10] and beat-to-beat variability).

Contrary to the commonly-used speckle tracking methods, our approach employs several principal differences. We are using optical flow estimation for tracking the points of interest instead of correlation between consecutive frames [1, 14]. Our experiments show that the tracking based on the pyramidal Lucas-Kanade feature tracker outperforms correlation approach.

However, the estimation of speckle movement is local only. The usage of generative probability shape model is used in order to preserve valid shape estimation of tracked LV. The left ventricle shape model was presented in [8]. The similar approach, where the probabilistic statistical shape model bases on PCA was employed, is described in [5]. However different per-point motion estimator is used [4]. Our probabilistic shape model comes from the is trained from the manually annotated data and from the programmatically computed local deformations of the myocardium. This deformations are computed using frequency modulation of the input control points.

2 Optical flow estimation

Our experiments shown that the Pyramid Lucas-Kanade (PyrLK) method [9] is a good choice for speckle motion estimation. The goal of the tracking is to find for given point $\mathbf{u} = (u_x, u_y)$ in image I corresponding point $\mathbf{v} = \mathbf{u} + \mathbf{d}$ in image J . There is the assumption that the neighborhood of the point \mathbf{u} is similar to the neighborhood of the point \mathbf{v} . The vector \mathbf{d} is referred as the image velocity or the optical flow at \mathbf{u} . It is defined as the vector that minimizes the function:

$$\epsilon(\mathbf{d}) = \epsilon(d_x, d_y) = \sum_{x=u_x-w_x}^{u_x+w_x} \sum_{y=u_y-w_y}^{u_y+w_y} (I(x, y) - J(x + d_x, y + d_y))^2 \quad (2.1)$$

The w_x and w_y define integration (neighborhood) window of size $(2w_x + 1) \times (2w_y + 1)$. Their typical values for are 2,3,4,5,6,7 and usually $w = w_x = w_y$.

There is a trade-off between local accuracy and robustness when choosing the integration window size. Smaller window size is able to capture even tiny motion. On the other hand, the tracking is lost when the movement exceeds the search window. Contrary, the large window size lacks accuracy. Therefore, an involvement of the image pyramid representation has been proposed in [2].

The image pyramid consists of the original image I^0 of size $n_x^0 \times n_y^0$ and L_m levels – usually 3. Each image I^L at level $L = 1, 2, \dots, L_m$ is resized, such its size is recursively set to $\frac{1}{2}n_x^{L-1} \times \frac{1}{2}n_y^{L-1}$. In the image pyramid perspective, the point \mathbf{u}^L is computed from the point in base image $\mathbf{u} = \mathbf{u}^0$:

$$\mathbf{u}^L = \frac{\mathbf{u}}{2^L} \quad (2.2)$$

The pyramidal tracking starts at the highest level image L_m . This will produce the optical flow estimation guess \mathbf{g}^{L_m-1} that is propagated to the next pyramid level L_{m-1} where the more correct flow estimation is computed.

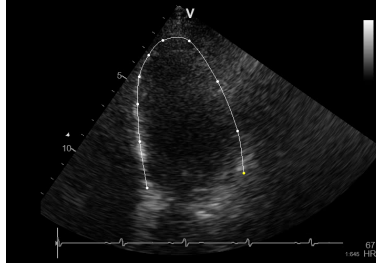


Figure 3.1: Manual annotation of mid-myocardium

This is repeated until the base pyramid level is reached. The general equation for estimating the optical flow at level L is:

$$\epsilon(\mathbf{d}^L) = \sum_{x=u_x-w_x}^{u_x+w_x} \sum_{y=u_y-w_y}^{u_y+w_y} \left(I^L(x, y) - J^L(x + g_x^L + d_x^L, y + g_y^L + d_y^L) \right)^2 \quad (2.3)$$

The initial guess $\mathbf{g}^{L_m} = (0, 0)$ and the propagation of the guess from level L to $L - 1$ is accomplished by $\mathbf{g}^{L-1} = 2(\mathbf{g}^L + \mathbf{d}^L)$. The final optical flow \mathbf{d} is calculated from partial flow estimation at the base level and the corresponding guess:

$$\mathbf{d} = \mathbf{g}^0 + \mathbf{d}^0 \quad (2.4)$$

3 Statistical shape model

The PyrLK point tracker provides robust technique for following individual points of interest. However, it lacks a binding between consecutive points of a shape. Therefore, it is important to maintain a specific shape of the LV during cardiac cycle. We are using a statistical shape model that has been previously described in [6, 7]. The main idea of statistical shape models is employment of probability density model. Some arbitrary shape $s = ((x_1, y_1), (x_2, y_2), \dots, (x_n, y_n))$ can be unambiguously represented as a column vector $\mathbf{s} = [x_1, y_1, x_2, y_2, \dots, x_n, y_n]^T$. Modeling of the shape variation is accomplished using Principal Component Analysis (PCA).

Our shape model takes into account several different origins of the shape variation. The first is the overall variability of LV shape during cardiac cycle as well shape difference between different subjects. The second origin of the shape variation is the thickness of the myocardium. The last origin of the shape variation is connected with the local strain in the myocardium.

The overall shape variation is modeled from the manually annotated data. 50 shapes from 4 LV cycles from 2 different subjects were annotated. The operator marked the points of the mid-myocardium and the Catnall-Rom spline [3] was interpolated between points (see Figure 3.1).

New points on the spline were established, such that the distances between consecutive points were uniform. All these uniformly distributed points were triplicated, such that the inner points represent endocardium and the outer points represent epicardium. Let the \mathbf{p}_i is some arbitrary mid-myocardium point. The \mathbf{p}_{i-1} is its predecessor and \mathbf{p}_{i+1} is its successor. The corresponding points $\mathbf{p}_{i \text{ inner}}$ and $\mathbf{p}_{i \text{ outer}}$ on the endocardium and epicardium respectively are:

$$\mathbf{p}_{i \text{ inner}} = \mathbf{p}_i - \frac{w \cdot \mathbf{n}}{2 \|\mathbf{n}\|} \quad (3.1)$$

$$\mathbf{p}_{i \text{ outer}} = \mathbf{p}_i + \frac{w \cdot \mathbf{n}}{2 \|\mathbf{n}\|} \quad (3.2)$$

where w is desired width of the myocardium and $\|\cdot\|$ represents Euclidean distance between consecutive points and \mathbf{n} is vector perpendicular to $\mathbf{p}_{i+1} - \mathbf{p}_{i-1}$. See Figure for more details.

The local variation of the strain among the myocardium is accomplished with the frequency modulation added to the uniformly distributed points. The distance between consecutive points is altered by different modulation

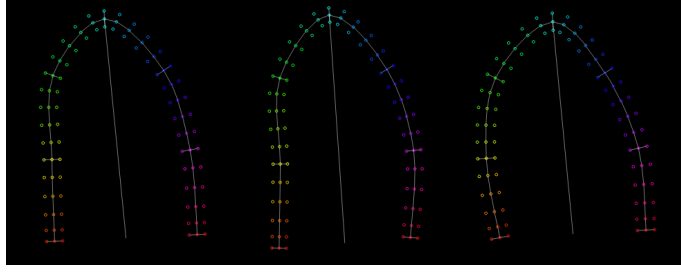


Figure 3.4: Mean LV shape (left) and some examples of its variation

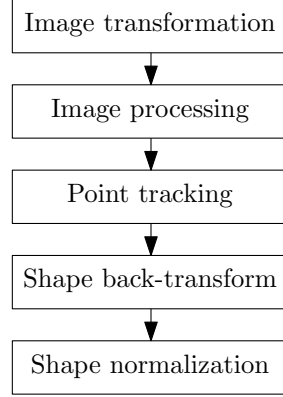


Figure 4.1: Algorithm pipeline

2. Covariance matrix \mathbf{S}

$$\mathbf{S} = \frac{1}{N-1} \sum_{i=1}^N (\mathbf{s}_i - \bar{\mathbf{s}})(\mathbf{s}_i - \bar{\mathbf{s}})^T \quad (3.6)$$

3. Compute the eigenvectors ϕ_1, \dots, ϕ_m and corresponding eigenvalues $\lambda_1, \dots, \lambda_m$ of \mathbf{S} .

4. Create projection matrix $\Phi = (\phi_1 | \phi_2 | \dots | \phi_t)$ that contains t largest eigenvalues from previous step ($t \leq m$). Usually, the t is selected to such value, that $\sum_{i=1}^t \lambda_i = 0.95 \sum_{j=1}^m \lambda_j$.

Now, every shape \mathbf{s} can be represented in t -dimensional PCA space:

$$\mathbf{b} = \Phi^T (\mathbf{s} - \bar{\mathbf{s}}) \quad (3.7)$$

Figure 3.4 shows mean calculated LV shape and some of its variations modeled with various vectors \mathbf{b} .

4 Algorithm description

Our tracking algorithm consists of individual function blocks where each block deals with a specific task and can be easily replaced with another block that solves the same problem, e.g., the image processing block can be empty or consists of several consecutive image filters. See Figure 4.1.

4.1 Image transformation and processing

The image transformation block transforms the input image from the input x - y coordinate system to the polar (angle-distance θ - d) coordinate system. The center of the θ - d coordinate system is placed to the center of the circular sector that contains B-mode image data (see Figure 4.2). An arbitrary point $X = (x, y)$ is thus transformed to the point $X' = (\theta, d)$, such:

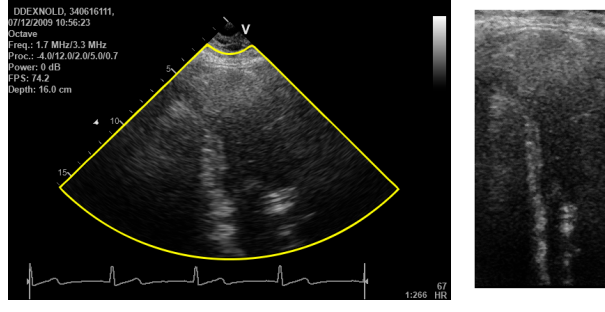


Figure 4.2: Image transformation from x - y coordinate system to the angle-distance (θ - d) coordinate system

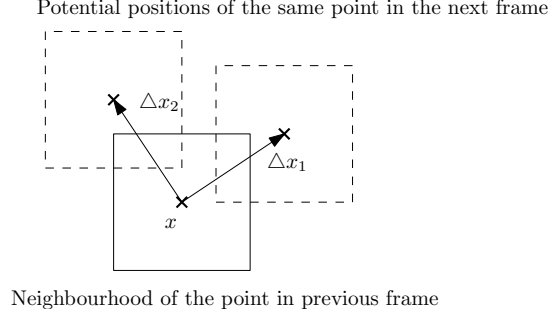


Figure 4.3: Point tracking using arbitrary metric

$$\theta = \text{atan2}(y, x) \quad (4.1)$$

$$d = \sqrt{x^2 + y^2} \quad (4.2)$$

The image processing block involves the application of image filters to the transformed frame. We have tested contrast enhancement, histogram equalization, edge detection, sharpening, and noise reduction in our experiments.

4.2 Point tracking

The point tracking block has three inputs - the previous frames, the annotated points within the previous frames, and the consecutive frame, where the point tracking algorithm should find the desired points. The consecutive frame is also processed with image transformation and filters. Additionally to the PyrLK point tracker, we have implemented speckle tracking based on the minimizing the Euclidean distance, correlation metric, cosine metric, or sum of absolute differences between the neighbor of tracked point in previous frame and potential position of the point in the next frame (see Figure 4.3). Let the pixel intensity neighborhood of the point x is denoted \mathbf{x} . The shift of the point x between the previous and the consecutive frame Δx is:

$$\Delta x = \arg \min_{i \in I} \|\mathbf{x} - \mathbf{x}_i\| \quad (4.3)$$

where \mathbf{x}_i is the pixel intensity neighborhood of the point x_i in the next frame and I is the set of all possible neighborhoods in the next frame.

Our algorithm also allows to have multiple weighted input frames. Suppose that we are estimating the LV shape in frame I_i . The input consist of j frames $(I_{i-j}, I_{i-j+1}, \dots, I_{i-1})$ with corresponding weights $\mathbf{w} = (w_j, w_{j-1}, \dots, w_1)$. Usually, the weights are set to $(w_1 = 1, w_2 = 0.5, w_3 = 0.25, \dots)$. The estimation of shape \mathbf{s}_i in frame I_i is then calculated from all previous frames. The weighted mean using weights \mathbf{w} is used to form the final shape.

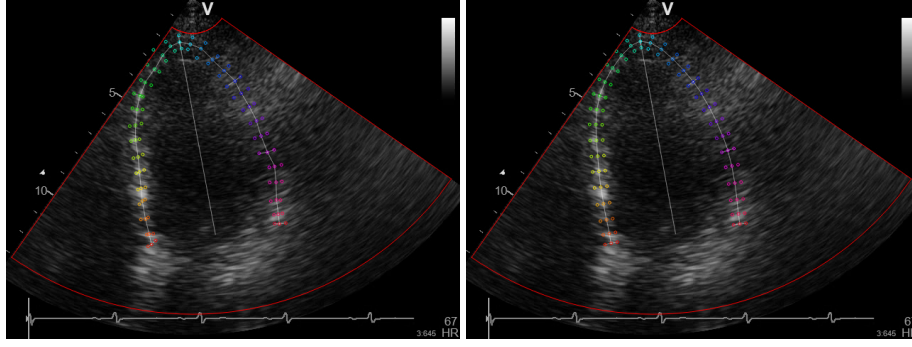


Figure 4.4: Points of the shape before normalization and after the PCA shape normalization

4.3 Shape back-transform and normalization

After all points in the next frame are located, the output shape is back-transformed to the x - y coordinate system. The next step is the employment of the statistical shape model. The shape is projected to the PCA subspace (eq. 3.7).

The task of the shape normalization is to find optimal projection vector \mathbf{b} that normalizes the input shape \mathbf{S} .

1. Initialize the projection parameters \mathbf{b} to zeros.
2. generate model instance $\mathbf{s} = \bar{\mathbf{s}} + \Phi \mathbf{b}$, where $\bar{\mathbf{s}}$ is the mean shape and Φ is the eigenvector matrix calculated from 3.6.
3. Find the optimal rotation and scale $T_{\theta,s}$ that transforms the \mathbf{s} to the input shape \mathbf{S} . See [7] for more details.
4. Apply the inverted transform $T_{\theta,s}^{-1}$ to the input shape: $\mathbf{S}' = T_{\theta,s}^{-1} \mathbf{S}$.
5. Project transformed shape \mathbf{S}' to the PCA subspace: $\mathbf{b} = \Phi^T (\mathbf{S}' - \bar{\mathbf{s}})$
6. On each component b_i of the vector \mathbf{b} apply the limit $\pm 3\sqrt{\lambda_i}$, where λ_i is the i th eigenvalue. This truncation ensures that the resulting shape will be similar to those in the original training set.
7. If the difference between previously calculated \mathbf{b} and current \mathbf{b} is greater than some threshold go to 2.
8. apply the last transformation $T_{\theta,s}$ to the generated model instance \mathbf{s} : $\mathbf{S} = T_{\theta,s} \mathbf{s}$

The result of the shape normalization is in Figure 4.4.

4.4 Result post-processing

The optional processing of the tracing result is the application of the simple moving average filter. The main parameter n of this filter is the floating window size that determines to which extent the data are smoothed. The arbitrary point p_i within shape i th shape \mathbf{s}_i is smoothed using average of the same points from different time indices $j \in \langle i - \lfloor \frac{n}{2} \rfloor, i + \lfloor \frac{n}{2} \rfloor \rangle$:

$$p_i \leftarrow \frac{\sum_{j=i-\lfloor \frac{n}{2} \rfloor}^{i+\lfloor \frac{n}{2} \rfloor} p_j}{n} \quad (4.4)$$

We have used this filter with the size parameter set to 1 (no filter), 3, 5, and 7.

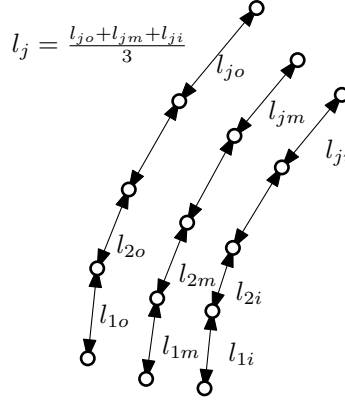


Figure 5.1: Per-point strain

5 Evaluation

5.1 Database description and performance metrics

TODO popsat zarizeni, ktery se vse skenovalo. We have tested our LV tracker on the dataset consisting of 10 subjects – 3 or 4 beat cycles were recorder for each subject resulting in total 36 beat cycles. The frame-rate ranges from 62FPS to 82FPS. The individual beat starts (EKG peaks) as well as the initial shape of the LV were manually annotated. For the shape annotation, just the mid-myocardium control points were annotated. The real LV shape was automatically deduced using the PCA shape model.

The longitudinal strain (main strain, *MS*) represents myocardial deformation along whole LV. The strain equation ϵ is defined as:

$$\epsilon = \frac{L - L_0}{L_0} \quad (5.1)$$

where L is the length of the LV after deformation and L_0 is the initial length of the LV. Our LV shape model consists of n mid-myocardial points – thus $3n$ in total. In order to estimate the main strain, individual per-point strains l_j have to be calculated ($j = 1, \dots, n - 1$). See Figure 5.1. The main strain is thus:

$$L = \frac{1}{n} \sum_{j=1}^n l_j \quad (5.2)$$

Our LV model is divided into six segments – see Figure 5.2. **TODO: Vlozit citaci, ze toto rozdeleni je standardni.**

There are several requirements of good tracker. Since the the LV myocardial movement is periodical, strain progress within each beat should be more or less the same – the beat-to-beat variance should be as low as possible. For one person/record, all strain progresses for all beats were aligned together and re-sampled to 100 values (see Figure 5.3). Beat-to-beat variance is thus the sum of standard deviations for each sample. We have measured the beat-to-beat variance for main LV deformations (main strain, *MS*) as well as for individual segments (per segment strain, *PSS*).

The beat-to-beat variance of two beats is standard deviation of absolute differences between re-sampled values. Let the strain values of the first beat are $\mathbf{v}_1 = (v_{1,1}, v_{1,2}, \dots, v_{1,m})$. The second beat values are $\mathbf{v}_2 = (v_{2,1}, v_{2,2}, \dots, v_{2,m})$, the differences are $\mathbf{d} = (|v_{1,1} - v_{2,1}|, |v_{1,2} - v_{2,2}|, \dots, |v_{1,m} - v_{2,m}|)$. The standard deviation and thus also the beat to beat variance between two beats is:

$$\sigma_{1,2} = \sqrt{\frac{1}{m} \sum_{i=1}^m (d_i - \mu)^2} \quad (5.3)$$

where μ is the mean value of \mathbf{d} . The PSS variation is similar to the MS variation, but only the points within specific segment are used for the estimation of the variation. For n beats the variation becomes:

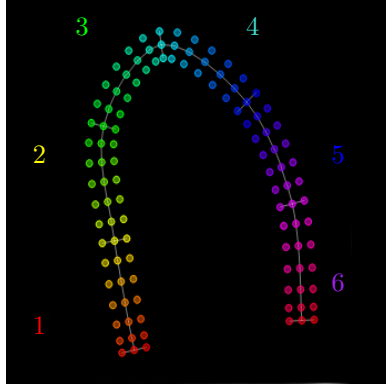


Figure 5.2: LV segmentation

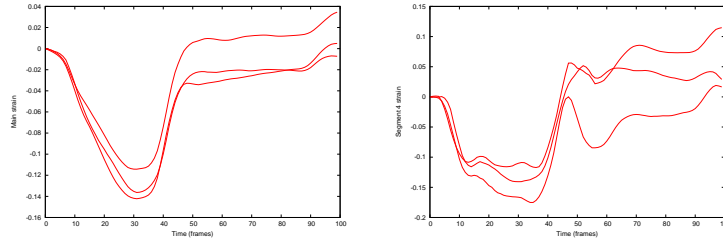


Figure 5.3: Beat-to-beat variance for main LV strain and for selected segment

$$\sigma = \frac{\sum_{i=1}^{n-1} \sum_{j=i+1}^n \sigma_{i,j}}{\binom{n}{2}} \quad (5.4)$$

The most important metrics of the tracker is precision. Since the movement of the LV is periodical, we can express the precision as the sum of quadratic differences of corresponding points from the first frame and the last frame of one beat. The shapes can't be compared directly, the last frame should be aligned (translation and rotation) to the first frame shape in terms of least square differences. Let the two aligned shapes are $\mathbf{s}_i = (\mathbf{p}_{i,1}, \mathbf{p}_{i,2}, \dots, \mathbf{p}_{i,m})$ and $\mathbf{s}_j = (\mathbf{p}_{j,1}, \mathbf{p}_{j,2}, \dots, \mathbf{p}_{j,m})$. The precision is the sum of square differences between corresponding points:

$$\text{precision} = \frac{1}{m} \sum_{k=1}^m \|\mathbf{p}_{i,k} - \mathbf{p}_{j,k}\|^2 \quad (5.5)$$

All algorithms were compared according to the following performance metrics:

- Main strain beat-to-beat variance
- Per-segment strain beat-to-beat variance
- Precision

5.2 Comparison of implemented techniques

As was mentioned in section 4, our LV tracking algorithm is modular. Individual components are easily interchangeable. We have compared the PyrLK-based point tracking technique with the simple tracker described in section 4.2. Out of the simple trackers based on the arbitrary distance metric, the best results were achieved with the cosine-based tracking technique. Therefore, in the following results, only the PyrLK and cosine trackers will be taken into account.

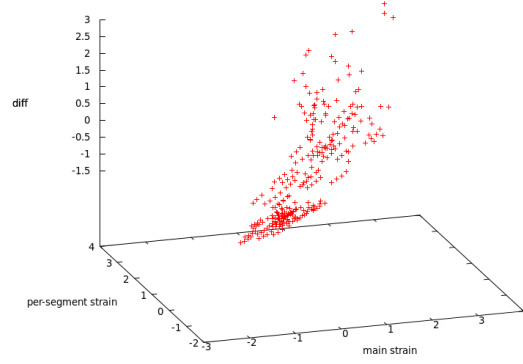


Figure 5.4: Distribution of normalized characteristics for compared LV trackers

The strain frequency modulation were performed with the following parameters – the frequency parameters $f = (1, 2, 3)$, phase shifts $\varphi = (0, \frac{1}{3}, \frac{2}{3})$, myocardial widths $w = (20, 30)$ pixels. Three overall myocardial shapes were trained. First was directly educed from the fore-mentioned parameters, the second and third LV shape models were trained in the similar way, only the amplitude of the modulation waves were reduced to 0.5 and 0.2 respectively. This modification of the training parameter causes more rigid model.

Our LV strain model consists of individual points divided into 6 segments. We have compared the models where each segment consists of 4, 6, and 11 mid-myocardial points. Thus the first model contains 57 points. The second model contains 93 points and the last model contains 183 points.

We have tested the following point-trackers:

- Tracking utilizing optical flow estimation (PyrLK)
 - Tracking individual points of the shape
 - Tracking all virtual points within certain neighborhood around each shape point. (kernel size 21×21 with one virtual point in every 3×3 sub-window)
- Tracking based on distance/similarity utilizing
 - Cosine distance (kernel 21×21)

The number of frames and corresponding annotations from which the LV motion is estimated was consecutively selected to 1 (no history), 2 with weights (1, 0.5), and 3 with weights (1, 0.5, 0.25). The post-processing averaging parameter n were set to (1, 3, 5, 7). It has emerged in our experiments that the image processing filters has no positive impact on the quality of tracking. Therefore, we have not included the image processing in batch testing.,

Nevertheless, the total number of tested individual trackers is 3 (frequency modulation, shape model stiffness) \cdot 3 (point count) \cdot 3 (point trackers) \cdot 3 (input frame weights) \cdot 4 (result averaging) = 324.

In order to find the best tracker, all three main characteristics (MS variance, PSS variance, and precision) have to be combined. For each characteristic c , we mean value μ_c and standard deviation σ_c and perform z-score normalization:

$$c' = \frac{c - \mu_c}{\sigma_c} \quad (5.6)$$

All three characteristics are summed and trackers can be directly compared. The better the tracker is, the lower is the sum of z-score normalized characteristics. The distribution of normalized characteristics for all compared LV trackers can be seen in Figure 5.4.

Table 1 shows the best 5 trackers according to the described characteristics. Several conclusions can be deduced from these results. First, the PyrLK-based trackers outperformed simple trackers based on the minimizing the distance between the neighborhood of tracked point and neighborhood around potential point position in consecutive frame – in our tests represented by trackers based on the cosine metric. Adding additional virtual points around each shape point does not have any positive impact on the tracking performance. The result processing

Table 1: The best trackers (all are PyrLK-based point trackers with modulation amplitude set to 0.2 and only one input frame)

Rank	Points per segment	moving average filter	Main strain Beat-to-beat variance	Per-segment beat-to-beat variance	Sum of square differences	Sum of normalized characteristics
1	11	7	0.0115	0.0264	19.3349	-4.8452
2	11	5	0.0119	0.0273	19.4738	-4.6489
3	11	3	0.0123	0.0283	19.3920	-4.4637
4	6	7	0.0122	0.0294	21.0413	-4.3603
5	11	7	0.0131	0.0279	20.1497	-4.2462

represented by the moving average filter improves the beat-to-beat variance as well as the target precision. However, too large smoothing parameter n may vanish some interesting details in myocardium movement. The direct impact of the of the moving average filter can be seen in Figure 5.4 as the quaternions aligned on the lines. It has also emerged that too high amplitude in local strain frequency modulation has negative impact on the beat-to-beat variance. The best results were achieved when the amplitude was set to 0.2. Adding additional weighted input frames to the tracking input does not improve the tracker performance. Our tests shows that better results are achieved when only one (last) frame is used when the optical flow of the points of interest in next frame are calculated.

6 Conclusion and further research

We have shown that the utilizing of the probability shape model and PyrLK-based point tracker outperforms simple trackers based on the correlation similarity. We would like to test our method on patients with myocardial movement disruption in our further experiments in order to prove that our method can be used to non-invasive examination and detection, e.g., the detection of myocardial ischemism.

References

- [1] Vera Behar, Dan Adam, and Peter Lysyansky. The combined effect of nonlinear filtration and window size on the accuracy of tissue displacement estimation using detected echo signals. *Ultrasonics*, 41(9):743–753, 2004.
- [2] Jean-yves Bouguet. Pyramidal Implementation of the Lucas Kanade Feature Tracker. Technical report, 2001.
- [3] Edwin Catmull and Raphael Rom. A class of local interpolating splines. *Computer aided geometric design*, 74:317–326, 1974.
- [4] Dorin Comaniciu. Nonparametric information fusion for motion estimation. In *Computer Vision and Pattern Recognition*, pages 59–66, 2003.
- [5] Dorin Comaniciu, Xiang Sean Zhou, and Sriram Krishnan. Robust real-time myocardial border tracking for echocardiography: an information fusion approach. *IEEE transactions on medical imaging*, 23(7):849–60, July 2004.
- [6] T. F. Cootes and C. J. Taylor. A mixture model for representing shape variation. *Image and Vision Computing*, 17(8):567–573, 1999.
- [7] T. F. Cootes and C. J. Taylor. Statistical models of appearance for computer vision. *Science and Biomedical Engineering, University of*, 2001.
- [8] G. Jacob, J.A. Noble, and A. Blake. Robust contour tracking in echocardiographic sequences. In *Sixth International Conference on Computer Vision*, pages 408–413. Narosa Publishing House, 1998.

- [9] B. D. Lucas and T. Kanade. An Iterative Image Registration Technique with an Application to Stereo Vision. In *Proceedings of Imaging Understanding Workshop*, volume 130, pages 121–130, 1981.
- [10] T. H. Marwick, R. L. Leano, and J. Brown. Myocardial strain measurement with 2-dimensional speckle-tracking echocardiography: definition of normal range. *JACC. Cardiovascular imaging*, 2:80–84, 2009.
- [11] J. Meluzin, L. Spinarova, and P. Hude. Estimation of left ventricular filling pressures by speckle tracking echocardiography in patients with idiopathic dilated cardiomyopathy. *European journal of echocardiography: the journal of the Working Group on Echocardiography of the European Society of Cardiology*, 12:11–18, 2011.
- [12] G. C. Nesbitt and S. Mankad. Strain and strain rate imaging in cardiomyopathy. *Echocardiography*, 29:337–344, 2009.
- [13] N. T. Olsen, P. Sogaardm, and B. W. Henrik. Speckle-tracking echocardiography for predicting outcome in chronic aortic regurgitation during conservative management and after surgery. *JACC. Cardiovascular imaging*, 4:223–230, 2011.
- [14] S.Y. Sokolov. Adaptation of speckle tracking algorithm for estimating global and regional left ventricular function. In *4th International Conference on Biomedical Engineering and Informatics (BMEI)*, volume 1, pages 88–90. IEEE, 2011.
- [15] J. Wang, J. M. Buerger, and K. Veerasamy. Delayed untwisting: the mechanistic link between dynamic obstruction and exercise tolerance in patients with hypertrophic obstructive cardiomyopathy. *Journal of the American College of Cardiology*, 54:1326–1334, 2009.